Research Article Vol. 13, No. 4 / April 2026 / Optica 669

OPTICA

Terawatt-level widely-tunable terahertz pulses from femtosecond laser-irradiated metallic foils

Jieya Ruan,[1,2] Xinyao Zhang,[1,2] Guoqian Liao,[1,2,3,*] Fangzheng Sun,[1,2] Yanyu Wei,[1,2] Hao Chen,[1,2] Yichen Dong,[1,2] Zhijie Qiu,[1,2] Jinguang Wang,[1] Yifei Li,[1] Xin Lu,[1,2,3] and Yutong Li[1,2,3,4]

[1]Beijing National Laboratory for Condensed Matter Physics, Institute of Physics, Chinese Academy of Sciences, Beijing 100190, China
[2]School of Physical Sciences, University of Chinese Academy of Sciences, Beijing 100049, China
[3]Songshan Lake Materials Laboratory, Dongguan, Guangdong 523808, China
[4]ytli@iphy.ac.cn
*gqliao@iphy.ac.cn

Received 13 October 2025; revised 20 January 2026; accepted 7 March 2026; published 1 April 2026

High-power tunable terahertz (THz) sources are highly desired for numerous applications. However, such sources with wide spectral tunability remain very lacking. Here we report on the highly efficient production of terawatt (TW)-level widely-tunable THz pulses, experimentally by harnessing the high-contrast sub-petawatt femtosecond laser impinging onto metallic foils. THz energy and autocorrelation measurements reveal the scaling-up of THz yield and the ultrabroadband tunability of THz spectra with the foil thickness. The THz peak power reaches up to ∼2 TW with the laser-to-THz energy conversion efficiency of ∼1%, and the THz center frequency is tunable across 3∼20 THz. Theoretical modeling together with measurements of escaping electrons explains the observed THz results, and attributes the THz spectral tunability to the controlled spatiotemporal dynamics of laser-accelerated energetic electrons with varying foil thickness. Single-shot THz-induced ionization damage of fused silica is presented as a proof-of-concept illustration of the ultrahigh THz intensity available. To the best of our knowledge, our results demonstrate a record-strong THz source spectrally-tunable across 3∼20 THz—a spectral region where the generation of intense sources has long been a formidable challenge before. Such an extreme THz source will not only open up avenues for the far-beyond-equilibrium control over matter, but also unlock the previously inaccessible relativistic THz optics.

https://doi.org/10.1364/OPTICA.581695

1. INTRODUCTION

High-power terahertz (THz) radiation sources are essential to many cutting-edge applications [1,2] such as the ultrafast control of matter [3–5], nonlinear optics [6,7] and compact particle acceleration [8]. Besides the high power, the THz spectral tunability is also a crucial figure of merit that is highly desired for numerous applications. For example, intense THz pulses with an appropriate spectral profile can resonantly excite and control specific collective modes of a certain degree of freedom in matter, such as the optical phonons in crystals [9,10], the vibrations of hydrogen-bonding network and the librations of molecules in the aqueous solution [11,12], and the rotations of protein molecules [13], whose characteristic frequencies span across a wide spectral range [14]. THz selective manipulation of degrees of freedom in matter is critical to the ultrafast material science, THz chemistry and biotherapy. Besides, the center frequency or wavelength of an intense light source is also recognized to have an important influence on the strong-field light–matter interactions, such as the ionization dynamics [15], the nonlinear propagation in media [16], and the generation of secondary radiation like x-rays [17]. Hence, the generation of THz sources with both high peak power and wide spectral tunability is not only of profound fundamental interest but also holds promise for applications.

Although great progress has been made recently in the THz science, widely-tunable intense THz sources, particularly in the spectral range of 5∼15 THz, are still very lacking. Given the difficulty in generation and the significance in applications, the 5∼15 THz spectral range has been labeled recently as the new "THz gap" that poses a major challenge for source development [18]. Conventional electron accelerators like the large-scale SLAC can output the sub-millijoule GW-level broadband THz radiation at high repetition rates with high stability [19]. Particularly, advanced free-electron laser (FEL) can deliver tunable narrowband THz radiation across a wide spectral range, but the THz peak power is limited to the MW ∼ GW level [20–23]. For crystal-based THz sources, multi-millijoule GW-scale single-cycle or multi-cycle low-frequency (<1 THz) THz pulses have been reported, respectively, by utilizing joule-scale femtosecond laser pulses to pump large-size cryogenically-cooled lithium niobate crystals [24] or periodically poled crystals [25–27]. Intense THz pulses in the spectral range of <5 THz can be generated from a

large-size organic crystal pumped by an infrared laser pulse at the 1.2∼1.6 μm wavelength [28–30]. Sub-millijoule 2-GW THz radiation at 15 THz has been reported recently with a 150-TW laser pulse pumping a large-area lithium niobate crystal, but it is not tunable in spectrum [31]. Although generation of narrowband pulses tunable in the range of 4∼18 THz is possible by difference-frequency generation in the nonlinear crystal [32,33], the THz peak power is limited below the MW level due to the low optical damage threshold of crystals. Laser-produced plasma is an alternative promising medium for generating high-power THz radiation [34]. It has been reported that ∼200-mJ TW-scale THz pulses can be generated by a 70-J picosecond laser pulse interacting with copper foils, with an efficiency of ∼0.3% [35]. Driving microchannel targets with 100s of joules of picosecond laser pulses has demonstrated a THz yield in the joule class [36]. It should be noted that despite some efforts to tune the THz spectra, the spectral content of picosecond laser-driven THz sources is limited to below 3 THz [35,37]. In contrast, femtosecond laser interactions with either solids [38–41], liquids [42], or gas-density plasmas [43–45] can produce THz pulses with ultra-broadband spectra at the repetition rate of the driving laser. For example, the THz radiation from two-color laser ionization of gases covers a spectral bandwidth up to 10s of THz, which is useful for spectroscopic applications [46]. It has been demonstrated that relativistic femtosecond laser pulses impinging on metallic foils can generate GW-level broadband THz pulses, with a laser-to-terahertz energy conversion efficiency in the level of ∼0.1% [38–41]. Nevertheless, previous studies focus primarily on the THz generation mechanisms and the THz yield, paying little attention to the THz spectral tunability.

Here, we demonstrate the efficient generation of extreme THz pulses with both an unprecedentedly high TW-level THz peak power and an ultrabroadband spectral tunable range across 3∼20 THz, from *high-contrast* sub-petawatt femtosecond laser interactions with thin metallic foils. To the best of our knowledge, this is the record-high-power THz source in the "THz gap" spectral region. Theoretical modeling and electron measurements explain the experimental results, and attribute the origin of spectral tunability to the distinct spatiotemporal dynamics of laser-accelerated electrons transporting in foils of different thickness. Single-shot THz-field-induced ionization damage of fused silica is observed as a proof-of-concept demonstration of such an ultraintense THz source.

2. EXPERIMENTAL SETUP

The experiment was conducted with the petawatt femtosecond Ti:sapphire laser system at the station D3 of the Synergetic Extreme Condition User Facility (SECUF). The laser delivered a 30-fs, 800-nm laser pulse at the maximum repetition rate of 1 shot/min. By the use of the cross polarized wave (XPW) generation technique, the laser temporal contrast ratio was $\sim 10^{-10}$ in the picosecond scale, avoiding the generation of large-scale plasmas and the destruction of thin foil targets prior to the arrival of the main laser pulse. Figure 1 sketches the experimental layout. The laser beam, focused with an off-axis parabolic mirror (f-number ∼3), was incident onto the foil target at an angle of ∼15° with respect to the target normal. This resulted in a full-width-at-half-maxima (FWHM) laser focal spot size of approximately 10 μm, and correspondingly, a peak intensity of $\sim 10^{20}$ W/cm^2 for the maximum 15-J laser energy and 0.5-PW peak power arriving at the target. The ps prepulse at the intensity of $\sim 10^{10}$ W/cm^2 would not damage the target [47]. Targets used in the experiment included the copper (Cu) foils with different thicknesses ranging from 5 to 300 μm and aluminum (Al) foils with thickness in the range of 20∼200 μm. The measurements were taken in single-shot mode. After each shot, the foil target was refreshed using motorized stages to ensure laser interacting with the intact foil with an equivalent size of >5 mm.

Given the rather large THz angular divergence, a gold-coated parabolic mirror was employed to collect and collimate the THz radiation emitted from the target rear side in the range of 24°∼87° with respect to the rear target normal. Passing through a 1 mm-thick diamond window that was of high spectrally-flat transmission in the whole THz range, the collimated THz radiation was relayed outside the vacuum chamber for measurements. The THz pulse energy was measured with a well-calibrated pyroelectric detector (Gentec-EO, THZ5I-BL-BNC). To avoid the saturation of detectors, broadband THz attenuators comprising high-resistivity silicon wafers and wire-grid polarizers were inserted in the THz path to weaken the THz radiation appropriately. The spectrally dependent energy transmittance of the diamond window, silicon wafers, and the relative spectral responsivity of the pyroelectric detector used are shown in inset (a) of Fig. 1. The THz focal spot was measured by replacing the pyroelectric detector with an uncooled microbolometer camera (SwissTerahertz, RIGI M2), showing a hollow ring-like intensity profile with a sub-mm size [see the inset (b) of Fig. 1]. For the THz spectral measurements, a customized non-collinear autocorrelator was used [48], enabling the single-shot spectral detection with an ultrabroadband response range and a high spectral resolution. A typical autocorrelation interferogram is shown in the inset (c) of Fig. 1.

Besides the THz radiation, the fast electrons escaping from the target rear side were also detected separately in some shots with an image plate (IP) stack placed ∼12 cm behind the target. Metallic and plastic filters of varying thicknesses were inserted in front of the IP and between IP layers to shield from the unwanted low-energy electrons, ions, and x-rays. Inset (d) of Fig. 1 illustrates a typical electron angular profile measured with the four-layered IP stack, from which one can infer the angular distribution, temperature, and total charge of the escaping electrons [49]. Measurements showed that the electrons were emitted primarily along the direction of 8° with a FWHM divergence angle of around 30°, roughly independent of the foil thickness. The electron divergence angle emitted from Cu foils was slightly larger than that from Al foils, as shown in the inset (e) of Fig. 1.

3. RESULTS AND DISCUSSION

A. THz Yield Characterization

We first evaluate the pulse energy of the collected THz radiation by taking into account the transmittance of optical elements in the THz path [see Supplement 1 for more details on the evaluation of THz energy]. Figure 2(a) shows the measured THz pulse energy and the corresponding laser-to-THz energy conversion efficiency, $\eta_{\text{l-THz}}$, for Cu or Al foils as a function of the foil thickness. The relative shot-to-shot fluctuation of THz energy is within 13%. As the foil thickness increases, the THz energy first decreases at 5 and 10 μm, then increases continuously from 20 μm onward, and exhibits a slight reduction at 300 μm. By contrast, measurements of ion acceleration under similar laser-foil parameters indicate a

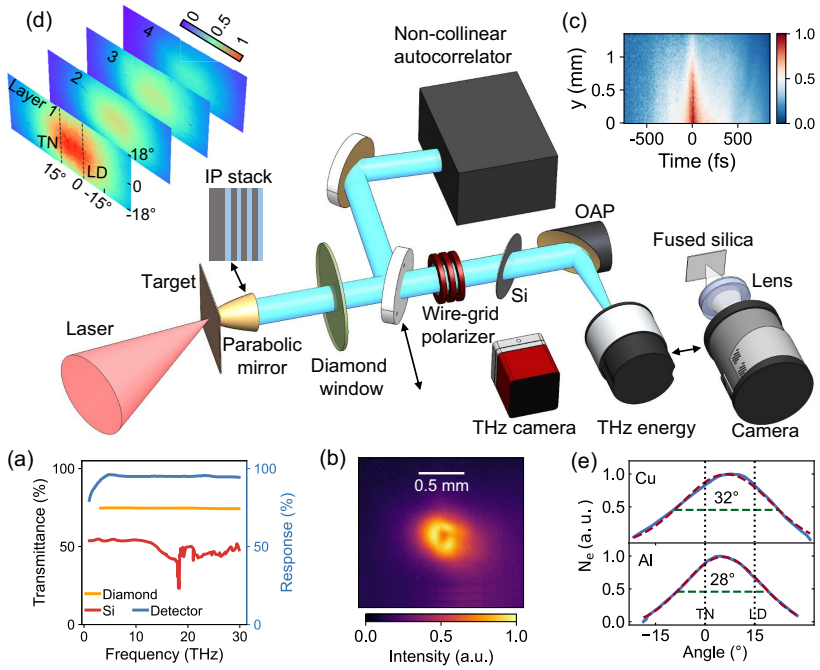

Fig. 1. Schematic of the experimental setup. Insets. (a) Spectrally dependent energy transmittance of the diamond window, silicon wafers in the THz path, and the relative spectral responsivity of the pyroelectric detector used. (b) THz focal spot measured for the 80 μm-thick Al foil. (c) Typical THz autocorrelation interferogram measured for the 20 μm-thick Cu foil. (d) Typical electron angular profiles measured with the four-layered image plate (IP) stack. (e) Angular distribution profiles, extracted from the IP measurements, of escaping electrons for 20 μm-thick Cu and Al foils. Black dotted lines in (d) and (e) mark the rear target normal (TN) and laser direction (LD), respectively. Red dashed curves in (e) represent the Gaussian fitting, and the green dashed line indicates the full width at half-maximum (FWHM).

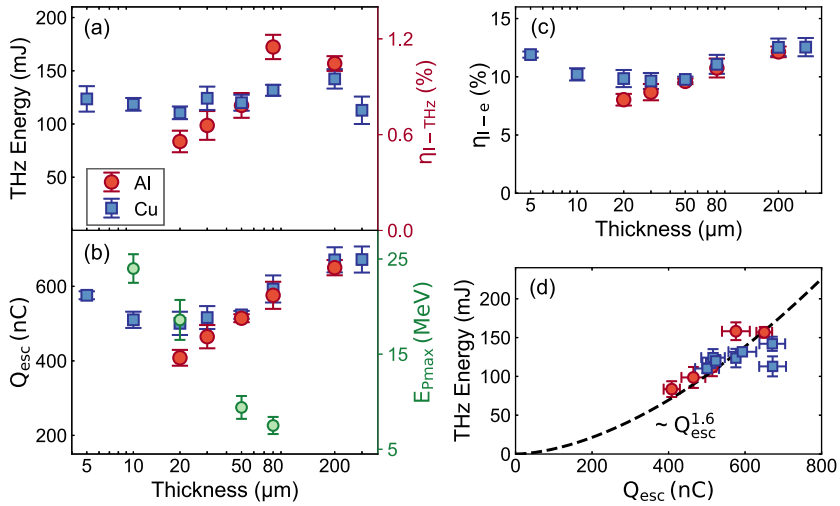

Fig. 2. THz energy and escaping electron measurements. (a) THz pulse energy and laser-to-THz energy conversion efficiency, $\eta_{l\text{-}THz}$, (b) escaping electron charge, Q_{esc}, and maximum proton energy, E_{pmax}, and (c) laser-to-electron energy conversion efficiency, $\eta_{l\text{-}e}$, as a function of the foil thickness for Cu (blue squares) and Al (red circles) foils. (d) THz energy versus Q_{esc} and power-law function fitting (dashed curve). The error bars represent the shot-to-shot fluctuation as at least three laser shots are taken for each foil thickness.

different dependency on the foil thickness. The maximum proton energy, E_{pmax}, drops significantly as the foil thickness increases [Fig. 2(b)]. It suggests that the THz pulse is mainly generated via the coherent transition radiation (CTR) of fast electrons traversing the metallic foil–vacuum interface, rather than the ion acceleration, which has been verified in previous studies [37,39,50]. It is also interesting to compare different foil materials. Cu foils produce higher THz energy than Al foils for thicknesses from 20−50 μm, while Al foils excel Cu foils in the THz energy for thicknesses ≥80 μm.

To understand the THz results, we have also retrieved the total charge, Q_{esc}, and the average temperature, T_e, of fast electrons escaping from the target rear side, based on the measurements with the IP stack. The laser-to-electron energy conversion efficiency, $\eta_{l\text{-}e}$, is evaluated approximately as $\eta_{l\text{-}e} = Q_{esc} k_B T_e/(e \cdot W_{Laser})$, where k_B is the Boltzmann constant and W_{Laser} is the laser energy. Figures 2(b) and 2(c) show the retrieved Q_{esc} and the evaluated $\eta_{l\text{-}e}$ as a function of the foil thickness, respectively. Q_{esc} is greater than 400nC, and $\eta_{l\text{-}e}$ is around 10%. Similar to the THz energy, the escaping electron charge shows first a decrease and then an increase

with increasing the foil thickness from 5 to 300 μm. This can be explained qualitatively as follows. The fast electrons, accelerated by the ultraintense laser pulse at the front surface of foils, transport forward with a rather large divergence angle, and establish a quasi-electrostatic sheath field at the foil rear surface, suppressing electrons to escape and resulting in ion acceleration. For thin foils whose thickness is less than the laser pulse length (∼10 μm), most of low-energy electrons are dragged back to the target by the strong sheath field. The refluxing electrons returning to the front surface will be reaccelerated back into the target by the intense laser field that still exists at the front surface. The laser re-acceleration of electrons leads to the enhanced $\eta_{l\text{-}e}$ and Q_{esc}, and as a result, gives rise to the increased THz energy at the 5 and 10 μm foil thickness. Similar THz energy boost at thin foils has been observed before [40]. For thick foils, the sheath field strength drops with the increased foil thickness due to the significant broadening of the electron beam size at the foil rear surface. The weakening of the sheath field allows more electrons to escape from the target, and consequently, inducing stronger THz radiation via CTR, despite that the broadened electron beam size could degrade the coherence of the high-frequency radiation [51]. This scenario is similar to our previous work [37], where the THz radiation was boosted by weakening sheath fields with the additional laser-produced preplasmas at the target rear surface.

Figure 2(d) shows the dependence of THz energy on the escaping electron charge. Fitting with the power-law function indicates a power index of ∼1.6, rather than the quadratic dependence commonly recognized in the CTR theory and observed in our previous work [37]. This deviation can be attributed to the broadened fast-electron beam size with the increased foil thickness, which degrades the coherence of the radiation field by each electron and reduces the electron-to-CTR conversion efficiency accordingly [51]. The influence of the fast-electron beam size on the CTR energy can also explain the THz results of different foil materials. Although Q_{esc} and $\eta_{l\text{-}e}$ for Cu foils remain slightly higher than those for Al foils at all thicknesses, the larger fast-electron divergence angle and beam size for Cu foils than those for Al foils [see inset (e) of Fig. 1] result in a gradually reduced electron-to-CTR conversion efficiency. Consequently, the THz energy from Al foils catches up and overtakes that from Cu foils at ≥80-μm thickness [see Fig. 2(a)]. In view of this, one can predict that the THz energy will eventually reduce at the sufficiently thick foils, as evidenced by the decreased THz yield observed at the 300 μm thick Cu foils.

The maximum THz pulse energy of ∼172 mJ is measured at the 100 μm thick Al foil, corresponding to a laser-to-THz energy conversion efficiency up to ∼1.15%. To our knowledge, this is the highest THz pulse energy driven by femtosecond laser pulses and the highest THz generation efficiency reported experimentally in the ultraintense laser–plasma interactions. Note that here we only consider the collected THz radiation that is available for practical use. The total THz energy emitted from the target rear surface can be evaluated roughly by taking into account the parabolic mirror's collection efficiency of ∼80%.

B. THz Spectral Tunability

We then investigate the THz spectral tunability with the noncollinear autocorrelation-based single-shot spectral measurements. Details on the calibration and data processing of autocorrelation interferograms can be found in Ref. [48]. Figures 3(a)–3(h) show the measured autocorrelation interferograms, the extracted autocorrelation traces, and the retrieved THz spectra at different foil thicknesses. The slight asymmetry in the autocorrelation traces could arise from the shot-to-shot fluctuation and the imperfect THz alignment. Despite the fact that the autocorrelation interferogram directly reflects the THz spectrum, one can still approximately evaluate the THz pulse duration, τ_{THz}, from the autocorrelation duration, τ_{AC}, as $\tau_{THz} = \tau_{AC}/\sqrt{2}$, by assuming a Gaussian-profiled THz waveform. This is reasonably true as both numerical simulations and modeling show the CTR pulse has a quasi-half-cycle waveform that resembles the fast-electron temporal distribution [52]. Figures 3(i) and 3(j) depict the retrieved τ_{THz} and THz center frequency, $\omega_c/2\pi$, as a function of the foil thickness, respectively. For ≥ 20-μm-thick foils, the measured autocorrelation interferogram exhibits as a single fringe, and the retrieved THz spectrum is broadband. As the foil thickness increases from 20 to 300 μm, τ_{THz} increases, and accordingly, the THz center frequency is tuned gradually from $\sim 5 - \sim 3$ THz. Additionally, τ_{THz} for Cu foils remains longer than that for Al foils. We ascribe the THz temporal-spectral tunability mainly to the broadened fast-electron beam size with the increased foil thickness. The CTR induce by an electron bunch is the coherent superposition of the fields produced by electrons at different spatiotemporal positions, i.e., as a result of the convolution of spatiotemporal properties of fast electrons. According to the theoretical modeling of CTR [51], τ_{THz} depends on both the electron bunch duration, τ_e, and the electron beam size, σ_e, approximately as $\tau_{THz}^2 \approx (\tau_e\delta)^2 + (\sigma_e \sin\alpha/c)^2$, where δ is the Doppler modification factor, α is the observation angle, and c is the light speed in vacuum, respectively. Due to the rather large divergence angle of the fast electrons during propagation through the foil, σ_e broadens with the foil thickness, and as a result, τ_{THz} increases and ω_c decreases with the foil thickness. Given the fact that the bunch duration of laser-accelerated electrons is comparable to the laser pulse duration ($\tau_e \approx 30$ fs) [51], one can quantitatively infer σ_e as a function of the foil thickness, L_f, from the measured τ_{THz} σ_e broadens approximately linearly with L_f, implying the ballistic transport of electrons in foils, as shown in the inset of Fig. 3(i). Linear fit indicates the electron beam divergence angle, θ, ∼31° for Cu foils and ∼26° for Al foils. These values are in line with the experimental measurements shown in the inset (e) of Fig. 1.

More interestingly, for the 5 and 10 μm thin foils, multiple periodic fringes appear in the autocorrelation interferogram, and correspondingly, the THz spectrum becomes relatively narrowband. When the foil thickness decreases from 10 to 5 μm, the center frequency is tuned from 8.8–20 THz, with a relative bandwidth, defined as the ratio of the FWHM bandwidth to the center frequency, $\Delta\omega/\omega_c$, of ∼28% and ∼16%, respectively. The dramatically increased THz durations and center frequencies [see the shaded region in Figs. 3(i) and 3(j)] cannot be explained simply by the CTR of a single electron bunch. This implies a transition in the dominant THz generation scenario. We attribute this exotic THz tunability to the fast-electron recirculation dynamics that occurs mainly when the target thickness is less than half of the pulse length [53]. Due to the high contrast ratio of the ultraintense laser pulse used in the experiment, strong sheath fields can be established both at the target front and rear surfaces. Most of fast electrons will be reflected back and forth by the sheath fields at both surfaces [40], and travel through the foil for multiple round trips,

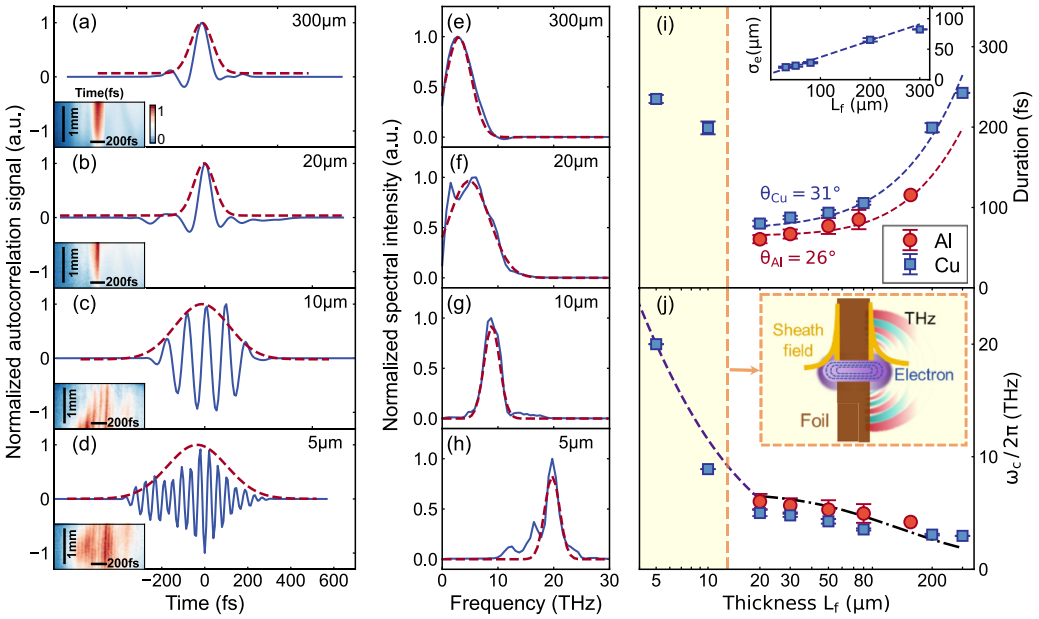

Fig. 3. THz autocorrelation measurements. (a-d) Measured THz autocorrelation traces, interferograms (inset), and (e-h) retrieved THz spectra at different Cu foil thickness. The horizontal and vertical black scale bars marked in the interferograms represent 200 fs and 1 mm, respectively. (i) Evaluated THz pulse duration, τ_{THz}, and (j) THz center frequency, $\omega_c/2\pi$ (blue squares for Cu and red circles for Al foils) as a function of the foil thickness, L_f, and theoretical fitting and calculations with the CTR modeling (dashed curves). The shaded region highlights the dominance of fast-electron recirculation dynamics. Inset in (i): electron beam size, σ_e, inferred from the measured τ_{THz}, as a function of L_f, and linear fit (dashed line). Inset in (j): schematic illustrating the recirculation-induced generation of multi-cycle THz radiation. For the foil thickness greater than 20 μm, τ_{THz} is numerically fitted with the equation, $\tau_{THz}^2 \approx (\tau_e\delta)^2 + (\sigma_e \sin\alpha/c)^2$, to infer the fast-electron divergence angle, θ, and then $\omega_c/2\pi$ is numerically calculated as $\omega_c/2\pi = 1/(2\tau_{THz})$ for the Cu foils, where $\tau_e \approx 30$ fs (approximately the same with the laser pulse duration), $\delta = 0.89$, $\sigma_e = \sigma_{e0} + 2L_f \cdot \tan(\theta/2)$, $\sigma_{e0} = 10$ μm (approximately the laser focal spot size), and $\alpha = 55°$ (approximately the middle angle of the THz collection angle range of 24°∼87°). For the foil thickness less than 20 μm, the theoretical modeling and fit parameters for $\omega_c/2\pi$ can be found in the main text and Supplement 1.

inducing multi-cycle narrowband CTR [51], as illustrated in the inset of Fig. 3(j). It should be noted that within the sub-picosecond recirculation duration, the foil target only undergoes sub-μm-scale expansion and remains substantially intact with little destruction. Hence, the foil surface can still be approximately modeled as a sharp metallic boundary during the electron recirculation. Because the electron beam size increases significantly and the sheath field strength reduces dramatically with the increased foil thickness, the electron recirculation behavior and the self-induced narrowband CTR dominates only at the thin foils. The resulting CTR has a center frequency approximately at $\omega_c/2\pi \sim 1/\Delta t_{rec}$, a duration of $\tau_{THz} \sim N_{rec} \cdot \Delta t_{rec}$, and a relative bandwidth of $\Delta\omega/\omega_c \sim 1/N_{rec}$, where N_{rec} is the recirculation number, and Δt_{rec} is the average time interval between successive recirculation, respectively. Δt_{rec} can be approximately calculated as twice the sum of the fast-electron transit time through foils ($\sim L_f/c$ for energetic electrons, where L_f is the foil thickness) and the dwell time, t_{dwell}, of electrons in the sheath fields (depends mainly on the sheath field strength, E_{sh}). By appropriately modeling Δt_{rec} and E_{sh}, one can numerically evaluate the THz center frequency as a function of the foil thickness. As shown in Fig. 3(j), the theoretical modeling is in good agreement with the experimental measurements. See Supplement 1 for details on the theoretical modeling and fit parameters used. These results imply that one can tune the THz spectra continuously in a wide range by manipulating the fast-electron spatiotemporal dynamics with varying the foil thickness appropriately.

C. THz Field-Induced Ionization Damage

THz radiation is generally recognized to be non-ionizing. To demonstrate the ultrahigh THz intensity and field strength available, we study the THz-field-induced ionization damage of optically-transparent solids. The THz pulse was focused onto a 1 mm thick fused silica wafer, and an imaging system equipped with a charge-coupled device (CCD) camera was placed in the THz propagation direction to monitor the fluorescence emitted from the fused silica [see the schematic in Fig. 1]. The THz peak power incident onto the sample was ∼0.3 TW with a center frequency at ∼5 THz, corresponding to a peak intensity of $\sim 7 \times 10^{13}$ W/cm^2 and a peak electric field of ∼2.4 V/Å. A strong flash of fluorescence from fused silica was captured by the camera during the THz irradiation, and after the single-shot THz irradiation, a sub-millimeter-sized damage pattern was clearly visible in the fused silica, as shown in Figs. 4(a)–4(c). These observations indicate that the THz pulse is strong enough to induce the irreversible damage of solid dielectrics at the single-shot mode. Given the fact that the band gap (∼9 eV) of fused silica is more than 400 times the THz photon energy, the damage could be resulted primarily from the THz field-induced tunneling ionization (rather than multiphoton ionization), then followed by the plasma expansion and thermal ablation on the nanosecond time scale. To the best of our knowledge, this is the first report on the single-shot THz field-induced ionization damage of silica.

It is interesting to note that both the damage pattern and the fluorescence profile show a hollow ring-shaped spatial distribution. This is because the CTR-induced THz pulse in our experiment is

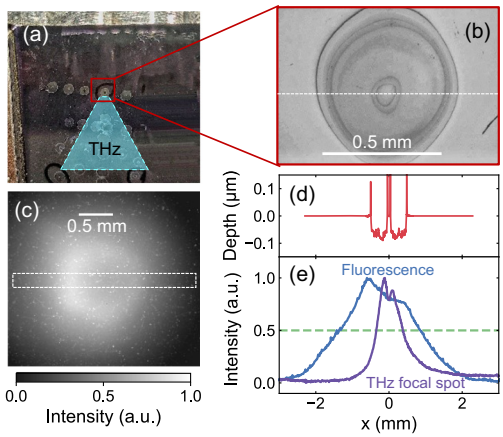

Fig. 4. THz-induced damage of fused silica. (a) Photograph and (b) optical microscope image of the fused silica after the single-shot THz irradiation. (c) Plasma fluorescence image captured by a CCD camera. (d) Depth morphology of the damaged area characterize with a white light interferometer. (e) Normalized line-out intensity profiles of the fluorescence image and THz focal spot.

approximately radially-polarized, and accordingly, the THz focal spot has a hollow ring-like intensity distribution, as evidenced by direct measurements with the THz camera [see inset (b) of Fig. 1]. Figures 4(d) and 4(e) depict the depth morphology of the damaged area, and the normalized line-out intensity profiles of the fluorescence image and THz focal spot, respectively. Quantitative size comparison indicates that the damage area is smaller than the THz focal spot. This suggests the extremely nonlinear behavior of field-induced ionization, i.e., the significant ionization damage only occurs in the region where the THz field is sufficiently high. In contrast, the fluorescence area is much larger than the THz focal spot. This could imply the outward lateral transport of electrons driven by sub-cycle radially-polarized THz fields and the THz-induced carrier multiplication [37,54] in the periphery of THz focal spot.

D. THz Figures of Merit

With the measured THz energy and the retrieved THz duration, one can evaluate the THz peak power, as shown in Fig. 5(a). The THz peak power rises at first and then gets saturated even reduces with the increase of foil thickness. The maximum peak power, P_{THz}, reaches ~2 TW at the 80 μm-thick Al foil. To the best of our knowledge, this is the first report on the femtosecond laser-driven TW-scale THz radiation. Based on the normalized ring-like intensity distribution, $I_0(x, y)$ of the THz focal spot measured [see inset (b) of Fig. 1], the THz peak intensity, I_{THz}, is inferred to be $\sim 4.8 \times 10^{14}$ W/cm^2 from the formula $P_{\mathrm{THz}} = \iint I_{\mathrm{THz}} \cdot I_0(x, y)\mathrm{d}x\mathrm{d}y$. The THz peak electric field is evaluated as $E_{\mathrm{THz}} = (2I_{\mathrm{THz}}/c\varepsilon_0)^{1/2} \sim 6.2$ V/Å, where c is the speed of light and ε_0 is permittivity. Accordingly, the normalized vector potential, as a critical parameter to characterize the electromagnetic field strength, is evaluated as $a_0 = eE_{\mathrm{THz}}/m_e c\omega_c \sim 1.1$, where the central frequency, $\omega_c/2\pi$, is ~5 THz, e and m_e are the charge and mass of the electron, respectively. This implies that the THz radiation produced in our experiment already arrives at the relativistic intensity [55] and enables the realm of relativistic THz optics, which was not accessible on a 100-fs-level half-cycle time scale previously.

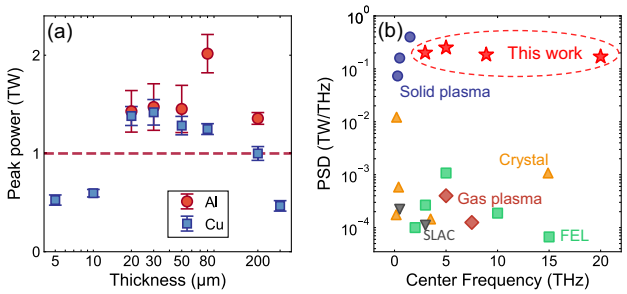

Fig. 5. THz peak power and power spectral density (PSD). (a) Evaluated THz peak power as a function of the foil thickness. (b) Comparison with state-of-the-art high-power THz sources. The data are referenced from previously experimentally reported records of THz sources based on conventional accelerators (gray down-triangles) [19], free-electron lasers (FEL, green squares) [20–23], optical rectification from crystals (orange up-triangles) [24–31], and laser-produced plasmas in solids (blue circles) [35–37] and gases (red diamonds) [43–45]. The red stars represent the results presented in this work.

Figure 5(b) illustrates the comparison with state-of-the-art high-power THz sources. Given the fact that those sources have different spectral bandwidths, the figure of merit used for comparison is the power spectral density (PSD), defined as the peak power divided by the FWHM spectral bandwidth. Almost all previously-reported THz sources of PSD >1 GW/THz are limited below 3 THz in the center frequency, based on either picosecond laser plasmas or large-size crystals. Sources with a PSD exceeding 1GW/THz in the range of 3~20 THz remain nearly blank. In contrast, the THz source demonstrated in our current work fills this long-standing gap. The PSD arrives at the unprecedentedly high level up to around 0.25TW/THz, more than 2 orders of magnitude higher than other existing advanced sources including the large-scale FEL. Furthermore, the THz center frequency is widely tunable across 3~20 THz while maintaining the ultrahigh PSD. Despite the single-shot operation and shot-to-shot instability, the THz source demonstrated here serves as a unique complement to widely-tunable intense THz sources.

4. CONCLUSION

We have experimentally demonstrated the highly efficient generation of ultrahigh-power spectrally-tunable THz pulses by a high-contrast femtosecond ultraintense laser interacting with metallic foils of varying thickness. Comprehensive THz characterization reveals not only the unprecedentedly high TW-level peak power and sub-TW/THz-scale power spectral density, exceeding other state-of-the-art THz sources by more than two orders of magnitude but also the ultrabroadband spectral tunable range across 3~20 THz. Theoretical modeling together with fast-electron measurements reproduces the experimental results and attributes the THz spectral tunability to the distinct fast-electron transport dynamics with varying foil thickness. The ultrahigh THz intensity and field strength available are illustrated by the single-shot THz-field-induced ionization damage of fused silica. Such a record-strong THz source tunable in the "THz gap" spectral region will unlock many intriguing opportunities in the extreme THz science [56]. On one hand, the TW-level THz peak power could allow access to a fully new paradigm of relativistic optics in the THz regime that has not been studied before, where many novel phenomena and new physics would be discovered [34,57].

On the other hand, the intense THz source with ultrawide spectral tunability will open up novel avenues for the THz control over matter by resonantly and selectively driving the specific collective modes to the far-from-equilibrium states. In combination with other ultrafast particle or photon beams generated concomitantly during laser–plasma interactions, such an extreme THz source will offer a unique pump–probe platform for studying light–matter interactions particularly irreversible phenomena.

Funding. National Key Research and Development Program of China (2024YFA1408703, 2021YFA1400204, 2021YFA1601700); National Natural Science Foundation of China (U24A2016, 12175306, 92250307, 12595363); Chinese Academy of Sciences (CAS) Project for Young Scientists in Basic Research (YSBR-059); CAS Youth Interdisciplinary Team (JCTD-2022-05).

Acknowledgment. This work was carried out at the Synergetic Extreme Condition User Facility (SECUF, [58]).The authors would like to acknowledge the staff at the SECUF for the laser operation and technical support.

Disclosures. The authors declare no conflicts of interest.

Data availability. Data underlying the results presented in this paper are not publicly available at this time but may be obtained from the authors upon reasonable request.

Supplemental document. See Supplement 1 for supporting content.

REFERENCES

1. A. Leitenstorfer, A. S. Moskalenko, T. Kampfrath, *et al.*, "The 2023 terahertz science and technology roadmap," J. Phys. D Appl. Phys. **56**, 223001 (2023).
2. P. Salén, M. Basini, S. Bonetti, *et al.*, "Matter manipulation with extreme terahertz light: progress in the enabling THz technology," Phys. Rep. **836**, 1–74 (2019).
3. T. Kampfrath, K. Tanaka, and K. A. Nelson, "Resonant and nonresonant control over matter and light by intense terahertz transients," Nat. Photonics **7**, 680–690 (2013).
4. X. Li, T. Qiu, J. Zhang, *et al.*, "Terahertz field–induced ferroelectricity in quantum paraelectric $SrTiO_3$," Science **364**, 1079–1082 (2019).
5. B. Ilyas, T. Luo, A. von Hoegen, *et al.*, "Terahertz field-induced metastable magnetization near criticality in $FePS_3$," Nature **636**, 609–614 (2024).
6. Y. Lu, Y. Huang, J. Cheng, *et al.*, "Nonlinear optical physics at terahertz frequency," Nanophotonics **13**, 3279–3298 (2024).
7. S. Li, G. Kumar, and T. E. Murphy, "Terahertz nonlinear conduction and absorption saturation in silicon waveguides," Optica **2**, 553–557 (2015).
8. W. R. Huang, A. Fallahi, X. Wu, *et al.*, "Terahertz-driven, all-optical electron gun," Optica **3**, 1209–1212 (2016).
9. A. S. Disa, J. Curtis, M. Fechner, *et al.*, "Photo-induced high-temperature ferromagnetism in $YTiO_3$," Nature **617**, 73–78 (2023).
10. J. Luo, T. Lin, J. Zhang, *et al.*, "Large effective magnetic fields from chiral phonons in rare-earth halides," Science **382**, 698–702 (2023).
11. H. Elgabarty, T. Kampfrath, D. J. Bonthuis, *et al.*, "Energy transfer within the hydrogen bonding network of water following resonant terahertz excitation," Sci. Adv. **6**, eaay7074 (2020).
12. P. K. Mishra, V. Bettaque, O. Vendrell, *et al.*, "Prospects of using high-intensity THz pulses to induce ultrafast temperature-jumps in liquid water," J. Phys. Chem. A **122**, 5211–5222 (2018).
13. X. Chen, H. Lindley-Hatcher, R. I. Stantchev, *et al.*, "Terahertz (THz) biophotonics technology: instrumentation, techniques, and biomedical applications," Chem. Phys. Rev. **3**, 011311 (2022).
14. D. N. Basov, R. D. Averitt, D. Van Der Marel, *et al.*, "Electrodynamics of correlated electron materials," Rev. Mod. Phys. **83**, 471–541 (2011).
15. P. B. Corkum, N. H. Burnett, and F. Brunel, "Above-threshold ionization in the long-wavelength limit," Phys. Rev. Lett. **62**, 1259–1262 (1989).
16. R. I. Grynko, G. C. Nagar, and B. Shim, "Wavelength-scaled laser filamentation in solids and plasma-assisted subcycle light-bullet generation in the long-wavelength infrared," Phys. Rev. A **98**, 023844 (2018).
17. J. Weisshaupt, V. Juvé, M. Holtz, *et al.*, "High-brightness table-top hard X-ray source driven by sub-100-femtosecond mid-infrared pulses," Nat. Photonics **8**, 927–930 (2014).
18. S. S. Dhillon, M. S. Vitiello, E. H. Linfield, *et al.*, "The 2017 terahertz science and technology roadmap," J. Phys. D Appl. Phys. **50**, 043001 (2017).
19. Z. Wu, A. S. Fisher, J. Goodfellow, *et al.*, "Intense terahertz pulses from SLAC electron beams using coherent transition radiation," Rev. Sci. Instrum. **84**, 022701 (2013).
20. G. N. Kulipanov, N. G. Gavrilov, B. A. Knyazev, *et al.*, "Research highlights from the Novosibirsk 400 W average power THz FEL," Terahertz Sci. Technol. **1**, 107–125 (2008).
21. M. Krasilnikov, Z. Aboulbanine, G. Adhikari, *et al.*, "First high peak and average power single-pass THz free-electron laser in operation," Phys. Rev. Accel. Beams **28**, 030701 (2025).
22. Y. Kang, T. Li, Z. Wang, *et al.*, "Continuous terahertz band coverage through precise electron-beam tailoring in free-electron lasers," Nat. Photonics **20**, 96–101 (2025).
23. Y. Liang, T. Li, J. Sun, *et al.*, "Superradiant terahertz free-electron laser driven by electron microbunch trains," Light Sci. Appl. **15**, 60 (2026).
24. X. Wu, D. Kong, S. Hao, *et al.*, "Generation of 13.9-mJ terahertz radiation from lithium niobate materials," Adv. Mater. **35**, 2208947 (2023).
25. S. W. Jolly, N. H. Matlis, F. Ahr, *et al.*, "Spectral phase control of interfering chirped pulses for high-energy narrowband terahertz generation," Nat. Commun. **10**, 2591 (2019).
26. F. Lemery, T. Vinatier, F. Mayet, *et al.*, "Highly scalable multicycle THz production with a homemade periodically poled macrocrystal," Commun. Phys. **3**, 150 (2020).
27. P. J. Dalton, C. T. Shaw, J. T. Bradbury, *et al.*, "Cryogenically cooled periodically poled lithium niobate wafer stacks for multi-cycle terahertz pulses," Appl. Phys. Lett. **125**, 141101 (2024).
28. C. Vicario, A. V. Ovchinnikov, S. I. Ashitkov, *et al.*, "Generation of 0.9-mJ THz pulses in DSTMS pumped by a $Cr:Mg_2SiO_4$ laser," Opt. Lett. **39**, 6632–6635 (2014).
29. M. Shalaby and C. P. Hauri, "Demonstration of a low-frequency three-dimensional terahertz bullet with extreme brightness," Nat. Commun. **6**, 5976 (2015).
30. C. Gollner, M. Shalaby, C. Brodeur, *et al.*, "Highly efficient THz generation by optical rectification of mid-IR pulses in DAST," APL Photonics **6**, 046105 (2021).
31. H. Kim, C. Kang, D. Jang, *et al.*, "Ionizing terahertz waves with 260 MV/cm from scalable optical rectification," Light Sci. Appl. **13**, 118 (2024).
32. B. Liu, H. Bromberger, A. Cartella, *et al.*, "Generation of narrowband, high-intensity, carrier-envelope phase-stable pulses tunable between 4 and 18 THz," Opt. Lett. **42**, 129–131 (2017).
33. F. Li, K. Zhong, J. Chi, *et al.*, "Ultra-widely tunable high-power terahertz parametric generation based on synchronized sub-nanosecond pump and nanosecond seeder," Optica **12**, 1391–1399 (2025).
34. G. Liao and Y. Li, "Perspectives on ultraintense laser-driven terahertz radiation from plasmas," Phys. Plasmas **30**, 090602 (2023).
35. G. Liao, H. Liu, G. G. Scott, *et al.*, "Towards terawatt-scale spectrally tunable terahertz pulses via relativistic laser-foil interactions," Phys. Rev X **10**, 031062 (2020).
36. G. Bruhaug, H. G. Rinderknecht, K. Weichman, *et al.*, "Joule-class THz pulses from microchannel targets," Opt. Lett. **49**, 1737–1740 (2024).
37. G. Liao, Y. Li, H. Liu, *et al.*, "Multimillijoule coherent terahertz bursts from picosecond laser-irradiated metal foils," Proc. Natl. Acad. Sci. U.S.A **116**, 3994–3999 (2019).
38. A. Gopal, S. Herzer, A. Schmidt, *et al.*, "Observation of gigawatt-class THz pulses from a compact laser-driven particle accelerator," Phys. Rev. Lett. **111**, 074802 (2013).
39. G.-Q. Liao, Y.-T. Li, Y.-H. Zhang, *et al.*, "Demonstration of coherent terahertz transition radiation from relativistic laser-solid interactions," Phys. Rev. Lett. **116**, 205003 (2016).
40. Z. Jin, H. B. Zhuo, T. Nakazawa, *et al.*, "Highly efficient terahertz radiation from a thin foil irradiated by a high-contrast laser pulse," Phys. Rev. E **94**, 033206 (2016).
41. H. Lei, F. Sun, T. Wang, *et al.*, "Highly efficient generation of GV/m-level terahertz pulses from intense femtosecond laser-foil interactions," Science **25**, 104336 (2022).
42. I. Dey, K. Jana, V. Y. Fedorov, *et al.*, "Highly efficient broadband terahertz generation from ultrashort laser filamentation in liquids," Nat. Commun. **8**, 1184 (2017).

43. L. Wang, Z. Zhang, S. Chen, *et al.*, "Millijoule terahertz radiation from laser wakefields in nonuniform plasmas," Phys. Rev. Lett. **132**, 165002 (2024).
44. T. Pak, M. Rezaei-Pandari, S. B. Kim, *et al.*, "Multi-millijoule terahertz emission from laser-wakefield-accelerated electrons," Light Sci. Appl. **12**, 37 (2023).
45. A. D. Koulouklidis, C. Gollner, V. Shumakova, *et al.*, "Observation of extremely efficient terahertz generation from mid-infrared two-color laser filaments," Nat. Commun. **11**, 292 (2020).
46. L. Bergé, K. Kaltenecker, S. Engelbrecht, *et al.*, "Terahertz spectroscopy from air plasmas created by two-color femtosecond laser pulses: the ALTESSE project," Europhys. Lett. **126**, 24001 (2019).
47. E. Atkočaitis, M. Jupé, Uė Kimbaraitė, *et al.*, "Exploring laser-induced damage threshold in metallic coatings across a fifteen-order-of-magnitude-range of pulse lengths," Opt. Express **33**, 44843–44857 (2025).
48. F. Sun, G. Liao, H. Lei, *et al.*, "A non-collinear autocorrelator for single-shot characterization of ultrabroadband terahertz pulses," Rev. Sci. Instrum. **93**, 123003 (2022).
49. D. R. Rusby, L. A. Wilson, R. J. Gray, *et al.*, "Measurement of the angle, temperature and flux of fast electrons emitted from intense laser–solid interactions," J. Plasma Phys. **81**, 475810505 (2015).
50. E. Denoual, L. Bergé, X. Davoine, *et al.*, "Modeling terahertz emissions from energetic electrons and ions in foil targets irradiated by ultraintense femtosecond laser pulses," Phys. Rev. E **108**, 065211 (2023).
51. G. Liao, F. Sun, H. Lei, *et al.*, "Femtosecond dynamics of fast electron pulses in relativistic laser-foil interactions," Phys. Rev. Lett. **132**, 155001 (2024).
52. A. S. Kuratov, A. V. Brantov, V. F. Kovalev, *et al.*, "Powerful laser-produced quasi-half-cycle THz pulses," Phys. Rev. E **106**, 035201 (2022).
53. Y. Sentoku, T. E. Cowan, A. Kemp, *et al.*, "High energy proton acceleration in interaction of short laser pulse with dense plasma target," Phys. Plasmas **10**, 2009–2015 (2003).
54. H. Hirori, K. Shinokita, M. Shirai, *et al.*, "Extraordinary carrier multiplication gated by a picosecond electric field pulse," Nat. Commun. **2**, 594 (2011).
55. G. A. Mourou, T. Tajima, and S. V. Bulanov, "Optics in the relativistic regime," Rev. Mod. Phys. **78**, 309–371 (2006).
56. X. C. Zhang, A. Shkurinov, and Y. Zhang, "Extreme terahertz science," Nat. Photonics **11**, 16–18 (2017).
57. X. Zhang, G. Liao, T. Xi, *et al.*, "Ionization-induced self-focusing of high-power terahertz pulses in gases," Phys. Rev. A **110**, 053519 (2024).
58. https://cstr.cn/31123.02.SECUF.D3.